POLITECNICO
MILANO 1863

RE.PUBLIC@POLIMI
Research Publications at Politecnico di Milano

Post-Print

This is the accepted version of:

G. Di Domenico, F. Topputo
Disturbances Quantification for Air-Bearing Spacecraft Attitude Simulation Platforms
in: AIAA Scitech 2024 Forum, AIAA, 2024, ISBN: 9781624107115, p. 1-23, AIAA 2024-0379
[AIAA Scitech 2024 Forum, Orlando, FL, USA, 8-12 Jan. 2024]
doi:10.2514/6.2024-0379

The final publication is available at https://doi.org/10.2514/6.2024-0379

Access to the published version may require subscription.

When citing this work, cite the original published paper.

Permanent link to this version
http://hdl.handle.net/11311/1259006

Disturbances Quantification for Air-Bearing Spacecraft Attitude Simulation Platforms

Gianfranco Di Domenico* and Francesco Topputo†
Politecnico di Milano, Milan, Italy, 20156

I. Introduction

Air-bearing joints have an extensive heritage in testing, verifying, and validating systems, algorithms, and configurations for large and small spacecraft. The working principle is based on the creation of a thin film of air that lifts the overlying platform, counteracting the effect of gravity, enabling at the same time its motion with minimal frictional effects. Examples of such technology are in [1–3]. [4] comprehensively reviews historical spacecraft simulators employing air-bearing joints.

In particular, spherical air-bearing joints enable the rotational movement of the overlying platform with 3 degrees of freedom (DoF); for this reason, they were traditionally associated with the development and testing procedure for spacecraft Attitude Determination and Control Systems (ADCS). However, despite such a technology being employed since the 1960s [5], there is minimal literature concerning the actual ability of such joints to faithfully emulate the conditions found in space. In particular, the «quasi-frictionless bearing» characteristic is rarely justified in literature and seldom proven by manufacturers. Moreover, the Earth's environment is characterized by additional disturbance torques that do not find a match in the space environment. In [5], a letter from the staff operating the attitude simulation platform at NASA Langley Center is reported; they explain their experience with the disturbances acting on the platform. Unfortunately, in the cited document, only a qualitative analysis is offered, and no quantitative analysis is found in the literature to our knowledge. This also depends on the fact that the characterization of the disturbances acting on a platform is usually performed on a case-by-case basis.

In this paper, the effect of mass unbalances, structural configuration, dynamics, aerodynamic design, electro-magnetic (EM) effects, and other minor sources of disturbance torques – such as battery discharge and radiation pressure – are assessed. The authors attemp to offer general analytical relationships to quantify the effect of the above-mentioned disturbances on a generic simulator based on an air-bearing spherical joint. Whenever necessary, the analyses have been performed considering three typologies of attitude simulation platforms: dumbbell, tabletop, and hollow (Figure 1) [4].

In the final part of the paper, practical issues related to the employment of such platforms in real-time hardware-in-the-loop simulations are discussed. In particular, the experience of STASIS (SpacecrafT Attitude Simulation System) [6], the platform under development at Politecnico di Milano to be used in the context of the EXTREMA (Engineering Extremely Rare Events in Astrodynamics for Deep-Space Missions in Autonomy) [7, 8], is reported. Particular focus is put in describing the issues related to the power system of the platform and the employability of wireless communication in real-time simulation environments.

(a) Dumbbell **(b) Tabletop** **(c) Hollow**

Fig. 1 Different topologies for attitude simulation platforms.

*PhD Student, Department of Aerospace Engineering and Research (DAER)
†Full Professor, Department of Aerospace Engineering and Research (DAER)

II. Disturbances analysis

When discussing about disturbances analysis, one should first clarify the actual meaning of the word *disturbance*. Wether an effect should be classified as a disturbance or not strongly depends on the simulation objectives and requirements. To make an example, the gravity gradient effects acting on an air-bearing platform could be classified as disturbances or not according to wether the objective of the simulation is the attitude evolution of a spacecraft in a LEO orbit or a deep-space attitude manouver. In the first case, the operator should realize that such effects are present even in the target environment and act upon the same physical phenomena; removing such effects when operating the air-bearing platform would be a modeling error or an approximation. On the contrary, deep-space cruises are not typically affected by gravity gradients, calling for the compensation and/or removal of such effects in the simulation environment. Of course, even in the former case one should make sure that, apart from the same mathematical expression for the gravity gradient torque, also the quantification of the effect (directly dependent on the platform inertial property, inherently different from the one of the spacecraft) should match the effects acting in LEO up to the desired error. A comprehensive review of the disturbances acting on such platform could be already found in [5]. The proposed characterization of disturbances was:

A) torques arising from platform (static and dynamic unbalance, anisoelasticity, material instability, gravity gradient, equipment motion);
B) torques from bearing (aerodynamics, exhaust air);
C) torques from environment (air damping and currents, magnetic fields, vibration, radiation pressure);
D) torque from test systems.

A. Structural disturbances

For what concerns the structural analysis, three main effects are considered: the static unbalance due to platform inertial properties, the first-order elastic deformation arising from the platform motion, and the dynamical structural response during typical maneouvers.

1. Static unbalance

The first effect to consider is a zero-order distance between the center of gravity (CoG) and the center of rotation (CoR) of the platform, resulting in undesired gravitational torques. In literature is it possible to find different commonly adopted strategies to mitigate such effects [9, 10]. High-fidelity computer-aided design (CAD) models are used to design the platform such that the effect is minimized, and symmetric configurations are preferred. However, it should be noted that for a general-purpose platform capable of hosting different kind of instrumentation, the testing payload and its distribution can have a significant influence on the mass properties, including the CoG position and the inertia tensor. Moreover, when employing off-the-shelf devices, it is not always possible to obtain high-fidelity CAD models from the manufacturers. More sophisticated strategies involve a set of moving masses and balancing algorithms that are able to compensate the CoG-to-CoR offset ([11–13]) for a range of platform configurations. Techniques empoyed as building block for such algorithms include, but are not limited to, batch observation [9, 14], Kalman filtering [14], and closed-loop control of the actuated masses [13]. In theory, provided that an ideal estimation of the CoG-to-CoR offset is provided, the accuracy of the balancing depends on the resolution of the actuation system employed. Stepper motors are commonly employed due to their easeness of integration and positioning accuracy. Three moving masses are the physical minimum to achieve balancing over three directions; however, having additional masses can be useful, for instance, to obtain a diagonal inertial tensor in a selected reference frame, or also to achieve a symmetric design for the platform that eases the balancing procedure. STASIS, the attitude simulation platform at Politecnico di Milano, is equipped with a set of 8 moving masses – two for the horizontal axes and four for the vertical axis (**Figure** 2). In order to remove the uncertainty associated to motor wires and cables during the motion of the mass, a custom motor controller board based on Trinamic's TMC2130 stepper motor driver and an ESP32-WROOM-32D/E wireless controller is embedded in the moving mass assembly itself. The board is able to sink power from the platform by a set of rolling contacts sliding on exposed conductive pads on the supporting surface, a custom printed circuit board (PCB) stiffened by the motor rail itself (**Figure** 2).

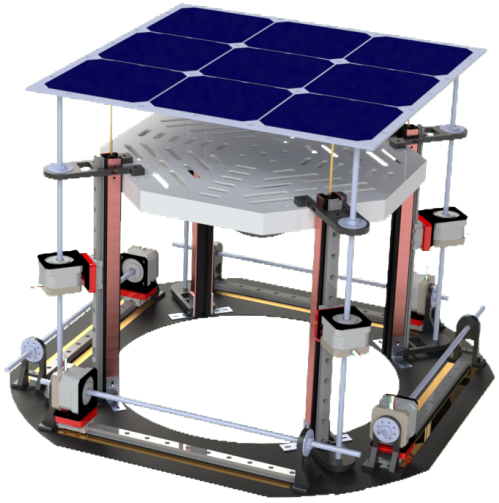

(a)

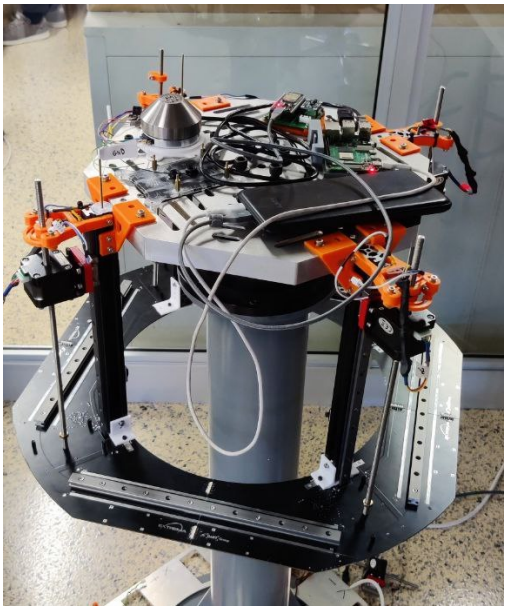

(b)

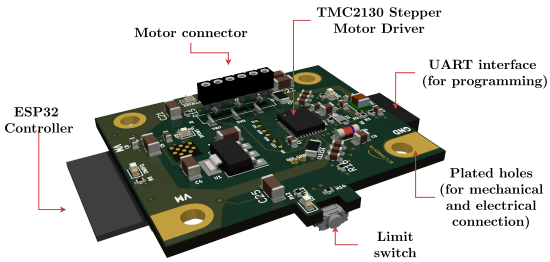

(c)

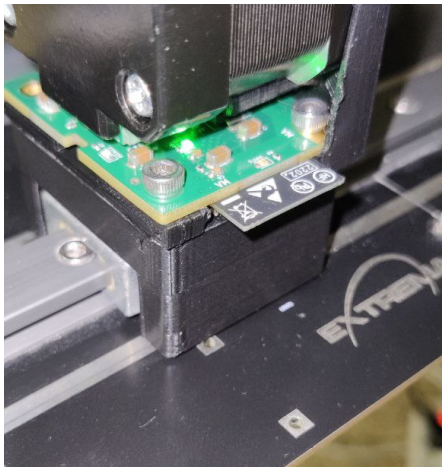

(d)

Fig. 2 (a) Rendering of STASIS (b) photo of STASIS during the development at Politecnico di Milano (c) 3D rendering of the stepper motor controller board (d) detail of the stepper motor sliding on the power rails

A mathematical expression for the single-axis residual unbalance due to the quantization of the position of a stepper motor can be obtained as:

$$T_d = \begin{cases} \frac{1}{2}\Delta\phi \cdot \frac{s_l}{360} \cdot m_m g_0 \cos\theta & \text{Horizontal} \\ \frac{1}{2}\Delta\phi \cdot \frac{s_l}{360} \cdot m_m g_0 \sin\theta & \text{Vertical} \end{cases} \quad (1)$$

T_d	=	disturbance torque [N m]
$\Delta\phi$	=	stepper motor angular resolution [deg/step]
s_l	=	screw lead [m]
m_m	=	moving mass [kg]
g_0	=	gravitational acceleration [m s^{-2}]
θ	=	platform tilt angle [deg]

The above formula takes into account the lead of the screw of the linear actuator, the angular resolution of the stepper motor, and the ratio between the actuated mass over total system mass. Microstepping has the potential to

significantly reduce the stepper motor resolution; however, specialized motor drivers are required, as microstepping is also known to reduce – especially for higher microstepping values – the stepper motor positional accuracy [15]. In the case of STASIS, the maximum positional accuracy is estimated to be at $1,79 \cdot 10^{-7}$ m, with a corresponding disturbance torque of $,23 \cdot 10^{-5}$ Nm. This does not take into account effect due to the mechanics of the stepper motor assembly, including backlash, screw slipping, and missed motor steps.

2. Elastic deformations

Even in the situation of perfect static compensation of the CoG, the elastic properties of the materials make any air-bearing platform suffer from attitude-dependent disturbances. Indeed, when performic static balancing, the assumption is that the platform is an infinitely rigid body whose geometric properties are immutable. While it is true that even space-born platforms are characterized by elastic deformation and disturbances, ground-based air-bearing attitude simulation platform are additionally subjected to elastic deformation due to their weight being sustained by the socket interface only. In other terms, any appendices not directly supported by the film of air is supported by the structural and elastic forces of the platform itself, leading to deformations. While this issue could be compensated with static balancind procedure at rest, the dynamic nature of the attitude configuration causes such deformation to be attitude-dependent. This effect is more pronounced in dumbbell-type platforms, as these have appendices far from the pressure actions that generate higher localized gravitational torques, resulting in a more prominent deformation and, therefore, a larger CoG shift. Assuming static balancing being performed in a null tilt angle, in [5] simple analytical laws relating the platform topology and orientation to the resulting disturbance torque are developed for dumbbell-style platforms:

$$T_d = g_0^2 l^2 [\sin(2\theta) - 2\sin(\theta)] \frac{12M_s^2 + 8M_s m_l + m_l^2}{24EI} \quad (2)$$

T_d	=	disturbance torque [N m]
g_0	=	gravitational acceleration [m s^{-2}]
l	=	length of main supporting beams [m]
θ	=	platform tilt angle [deg]
M_s	=	mass of the end-arm instrumentation [kg]
m_l	=	total mass of supporting beam [kg]
EI	=	bending stiffness of beams [N m^2]

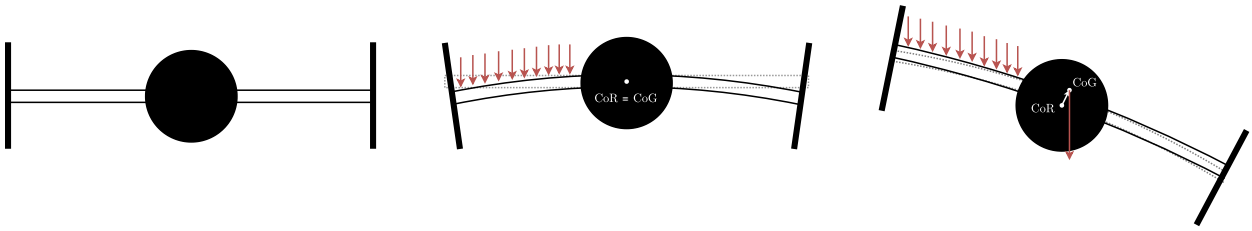

(a) Ideal **(b) Flexed/Balanced** **(c) Rotated**

Fig. 3 CoG shift on rotation due to flexural displacements for dumbbell configuration

The same reasoning can be applied to the tabletop topology. In this case, however, the topology does not foresee external horizontal appendices. Therefore, one can assume that, at null tilt angle, the static balancing is equivalent in the hypothesis of elastic and rigid body. However, upon rotating, the vertical-axis counter-balancing appendices exhibit flexion due to the fact that the gravitational forces are not parallel anymore to their dominant dimension. Neglecting tensile displacements, one can easily apply the same methodology of before, modeling the appendices as linear beams with fixed cross-sectional inerta. In a generic tilted condition, the following expression for the disturbing torque is obtained:

$$T_d = \frac{g_0^2 l^2 m_l^2 \sin(2\theta)}{48EIN_l} \quad (3)$$

T_d	=	disturbance torque [N m]
g_0	=	gravitational acceleration [m s^{-2}]
l	=	length of the counterbalance beam masses [m]
θ	=	platform tilt angle [deg]
m_l	=	total mass of counter-balance beam masses [kg]
EI	=	bending stiffness of the supporting beams [N m^2]
N_l	=	number of counter-balance beam masses

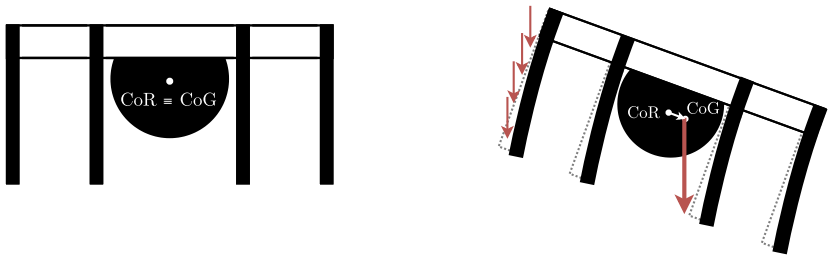

(a) Ideal **(b) Rotated**

Fig. 4 CoG shift on rotation due to flexural displacements for tabletop configuration

In this case, the only dependence is on the double of the rotational angle. This is explained by noticing that a tabletop configuration, under the assumption of rigid plate, has no initial deflection and, therefore, there is no "rebound effect" from the original condition at $\theta = 0$. Again, the direction of the perturbing torque is coherent with the tilt angle direction for $\theta < 90$ deg. As most tabletop configurations are bounded under 60 deg, this means that the perturbing torque tends to move the platform towards the end-course, with a peak at 45 deg. **Figure** 5 shows the trend of the normalized disturbance torque for the two configuration for the two platforms, assuming perfect static balancing at null tilt angle.

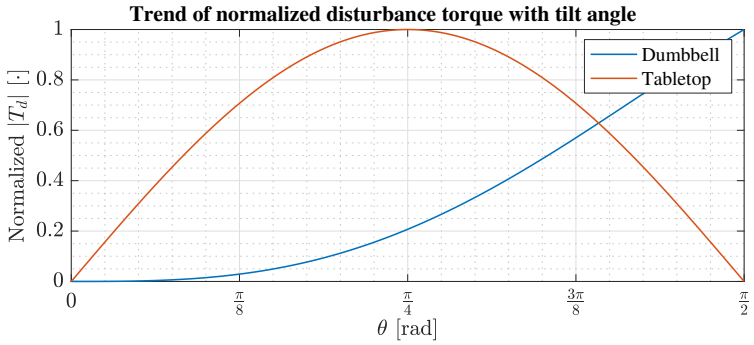

Fig. 5 Normalized disturbance torque module with the tilt angle for the dumbbell and tabletop configurations

Concerning the hollow sphere configuration, from the elastic structural standpoint it is clearly the best option to minimize the residual elastic torque. Indeed, the general topology foresees no flexible appendices and therefore any rotation has little to no effect on the center of mass. Of course, such features comes at the cost of having an exploitable surface much smaller compared to other configurations.

3. Dynamical structural response

The analysis of the dynamical effects has been deferred to further works. According to the initial disclaimer on the definition of disturbance, one should consider two different effects:

- the dynamic responses with a physical equivalent in the simuland (i.e., the appendices of a dumbbell-type platform could mimic the effects of deployed solar panels). These should not be considered disturbances unless a perfect quantitative equivalence is desired;
- dynamic responses with no physical equivalent. These could arise, for instance, due to a residual unbalance or divergent topologies between the simuland and the simulator

In order to be significant, such analyses should take into account the effect of typical maneouvers. In general, it is expected such effect to be negligible with respect to the static errors in the long run due to the periodicity of structural vibration and the higher frequency involved (assuming rigid platforms).

B. Aerodynamics

Regarding the aerodynamic sources of disturbance, it is convenient to logically split the effects into: a) the interaction of the spherical interface with the socket; and b) the interaction of the platform itself with the surrounding air.

1. Air bearing effects

The former effect consists primarily of skin friction between the sphere and the socket. Air-bearing can procude air films as thin as 1 μm [16], resulting in shear effects due to closely spaced boundary layers.

The gasdynamics effect of gas-bearing joints have been extensively studied in tribology. Indeed, such configurations are not only typical of attitude simulation platform, but also of other industrial applications (i.e., [17, 18]) and natural structures (such as human joints [19]). However, the external conditions (such as the effect of the weight as a static load, or the absence of out-of-plane excitation) are typical of space applications. The theory on such effect date back to Reynolds lubrication theory [20, 21], in which the flow field through a small channel is studied. The assumption here is that, up to certain Reynolds numbers, the flow can be assumed laminar [22] and that the viscous forces dominate over the inertial ones. Such assumptions can be assumed true even in the case of spherical bearings. A more recent study of such effects is given in [16, 23]. Differently from the classical Reynolds formulation, the effect of the orifice thorugh which compresses gas is pumped has a primary effect. [16] shows how such effect is actually at the foundation of the concept of the bearing. The relation between the film thickness and the applied external load is explained in terms of static pressure after the orifice. Indeed, when an external weight is applied, the outcoming flow is found at a higher pressure; the static pressure proceeds to decrease gradually up to the end of the socket. Higher load values correspond to smaller film thicknesses since a smaller channel results in increased pressure (and therefore, an increased ability to withstand the upper flow). This ideal behavior, of course, is affected by manufacturing tolerances (expecially in terms of surface roughness and spherical eccentricity) and other phenomena (such as air hammering). In general, once the flow field is solved, one can compute the following charasteristics for the joint:

$$\text{Load capacity} := F_L = \iint_{\text{SS}} -p_s(r,\theta,\phi)(\hat{\vec{n}}_A \cdot \hat{\vec{n}}_z)dA \tag{4}$$

F_L = load capacity of the bearing [N]
p_s = static pressure distribution [Pa]
$\hat{\vec{n}}_A$ = surface normal [$\cdot$]
$\hat{\vec{n}}_z$ = vertical axis direction [$\cdot$]
SS = spherical surface within the socket [$\cdot$]
dA = infinitesimal area element of sphere [m^2]

$$\text{Drag torque} := \vec{T}_d = \iint_{A_v} \vec{r} \times \vec{\tau}_\mu(r,\theta,\phi)dA \tag{5}$$

$\vec{T}_d$ = drag torque [N]
$\vec{r}$ = distance vector with respect to reference point [m]
$\vec{\tau}_\mu$ = viscous stress at surface [N m^-2]
A_v = viscous area considered [$\cdot$]
dA = infinitesimal area element of sphere [m^2]

Both formula require the knowledge of the flow field in order to be solved. In literature, analytical solutions to the flow field problem under simplifying assumptions have been proposed [20, 23, 24]. Analytical solutions are also available for more complex cases; however, the general formulations found have been considered either not applicable to the air-bearing spherical joint problem or too complex for a straightforward implementation. It should be noted that the literature in regards in quite scattered, especially because the configuration of the orifices and the type of inlet heavily influence the characteristics of the flow field.

For what concerns the load capacity, the simplifying assumption at the foundation of the standard Reynolds lubrication theory can be used. In particular, the critical simplification lies in the assumption of constant static pressure along the channel width, and a linearly-varying trend from the inlet pressure to the outlet pressure. The outlet pressure can be safely assumed equal to the ambient pressure for low velocities of the flow. In this case, the expression for the pressure at the spherical interface can be assumed as:

$$p_s(r,\theta,\phi) = p_i + (p_a - p_i)\frac{\theta}{\theta_S} \tag{6}$$

p_i = inlet pressure [Pa]
p_a = ambient pressure [Pa]
θ_S = angular half-extension of the spherical socket [rad]

In the simple case of a single orifice, literature seems to adhere to this simple model; a more accurate analysis is given in [23], where the linear trend is assumed only at a certain distance from the inlet. The same reference suggests that the inlet pressure differs from the total pressure of the fluid, and introduces additional pressure quantities such as the *theoretical inlet pressure* p_t, corresponding to a linear extrapolatino of the pressure as found in the viscous region. As the entrance area is typically small compared to the channel length, it is considered safe to assume the inlet pressure equal (or proportional through a constant reduction coefficient k_p between $0.8 - 0.9$) to the total pressure, knowing that the resulting figure will only be a ballpark estimation of the load capacity of the bearing. Under such an assumption, the overall formula for the load capacity can be written, under the hypothesis of axysimmetric fluid flow, as:

$$\begin{aligned} F_L &= \int_0^{2\pi} \int_0^{\theta_s} [k_p p_t + (p_a - k_p p_t)\frac{\theta}{\theta_s}] R_S^2 \sin\theta \mathrm{d}\theta \mathrm{d}\phi = \\ &= 2\pi R_S^2 \left[\int_0^{\theta_s} k_p p_t \sin(\theta) \mathrm{d}\theta + \int_0^{\theta_s} (p_a - k_p p_t)\frac{\theta}{\theta_s} \sin(\theta) \mathrm{d}\theta \right] = \\ &= 2\pi R_S^2 \left[k_p p_t (1 - \cos(\theta_s)) + (p_a - k_p p_t)\frac{\sin(\theta_s) - \theta_s \cos(\theta_s)}{\theta_s} \right] = \\ &= 2\pi R_S^2 \left[k_p p_t \left(1 - \frac{\sin\theta_s}{\theta_s}\right) + p_a \left(\frac{\sin(\theta_s)}{\theta_s} - \cos(\theta_s)\right) \right] \end{aligned} \tag{7}$$

In case $p_t \gg p_a$,

$$F_L \simeq 2\pi R_S^2 k_p p_t \left(1 - \frac{\sin\theta_s}{\theta_s}\right) \tag{8}$$

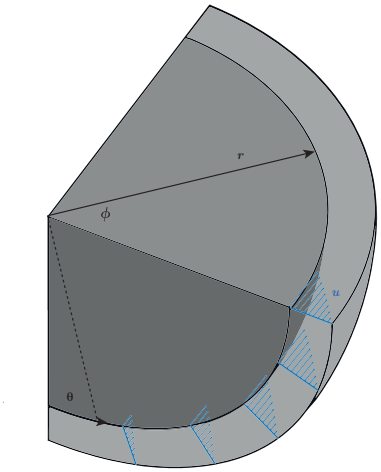

Fig. 6 Geometry and fluid flow assumption under the considered hypothesis. Notice that only the ϕ component of the velocity is depicted.

Regarding the drag torque, a simple analytical model can be derived under the same simplifying assumption. Symmetry considerations allow the expression of the problem in an axysimmetric reference frame, in which the no-slip boundary condition on the sphere make each pathline cover a spiraling motion. Referring to **Figure** 6, for a pure z-axis rotation, a first-order model for a smooth, single-orifice air-bearing yields a linear profile for the out-of-plane component of the fluid flow velocity. In particular, the no-slip condition at the film-sphere interface results in an analytical expression of the out-of-plane velocity as [25]:

$$v_\phi(r, \theta, \phi) = \frac{\omega_z R_1^3 (r^3 - R_2^3)}{r^2 \left(R_1^3 - R_2^3\right)} \sin\theta \tag{9}$$

The sphere velocity can be marked as

$$v_\phi|_{R_1} = \omega_z R_1 \sin\theta \tag{10}$$

so, eq. (9) becomes:

$$v_\phi(r,\theta,\phi) = v_\phi|_{R_1} \cdot \frac{R_1^2}{r^2}\frac{r^3 - R_2^3}{R_1^3 - R_2^3} \tag{11}$$

The cubic differences can be approximated in the narrow channel using Taylor expansion. Indeed,

$$(x^3 - c^3) \simeq (x^3 - c^3)|_{x=c} + 3x^2|_{x=c}(x-c) + O((x-c)^2) = 3c^2(x-c) \tag{12}$$

Taking r as variable and R_2 as constant,

$$v_\phi(r,\theta,\phi) = v_\phi|_{R_1} \cdot \frac{R_1^2}{r^2}\frac{3R_2^2(r-R_2)}{3r_2^2(R_1-R_2)} \tag{13}$$

Note that the $(R_1 - R_2)$ quantity is nothing less than the channel width t.
Considering that, $\forall r \in [R_1, R_2] \quad r \simeq R_1 \simeq R_2$, the equation simplifies to:

$$v_\phi(r,\theta,\phi) = \underbrace{v_\phi|_{R_1}}_{\text{Sphere velocity}} \cdot \overbrace{\frac{(r-R_2)}{t}}^{\text{Linear decay}} \tag{14}$$

From the above expression, the shear stress at the wall can be written as:

$$\tau_\phi = \mu \frac{v_\phi|_{R_1}}{t} \tag{15}$$

And therefore, the ϕ component of the force acting on an infinitesimal surface of the sphere is written as

$$dF_\phi = -\mu \frac{v_\phi|_{R_1}}{t} dA = -\mu \frac{v_\phi|_{R_1}}{t} R^2 \sin\theta \mathrm{d}\theta\mathrm{d}\phi \tag{16}$$

Replacing the expression for the sphere surface velocity, and assuming the viscous area equivalent to the entire socket are, the magnitude of the drag torque can be evaluated as:

$$\begin{aligned} |T_{\text{drag}}| &= \int_0^{2\pi}\int_0^{\theta_s} (R_S \sin\theta) \cdot \left(-\mu \frac{\omega_z R \sin(\theta)}{t}\right) R^2 \sin\theta_s \mathrm{d}\theta\mathrm{d}\phi = \\ &= -2\pi \frac{R_S^4}{t}\mu\omega_z \int_0^{\theta_s} \sin^3\theta_s \mathrm{d}\theta = \\ &= -\frac{\pi R_S^4 \mu\omega_z}{6t}\left[\cos(3\theta_s) - 9\cos(\theta_s) + 8\right] \end{aligned} \tag{17}$$

Notice that the viscous area can be different from the contact area due to the presence of the orifice that determines flow regions whose description cannot be fit under the assumption of simple axysimmetric fluid flow. However, we consider it a good first-order approximation to analyze the effect of aerodynamic drag on the sphere-socket due to shear.

Model validation

In order to validate the relations obtained above, we have referred to the datasheets of the SRA series of air-bearing spherical joint manufactured by Specialty Components. The choice was performed due to the fact that there is a structured database of spherical air-bearings containing the information on the film thickness, maximum load capacity, inlet pressure, and expected drag torque at 30 rpm. The data on the geometry and the datasheet values for the load capacity and drag torque at 30 rpm have been collected and imported into MATLAB. Then, the geometry information was used to appy eq. (7) and eq. (17) and obtain the predicted values. Then, the values have been plotted against their datasheet counterpart. The results are shown in **Figure** 7.

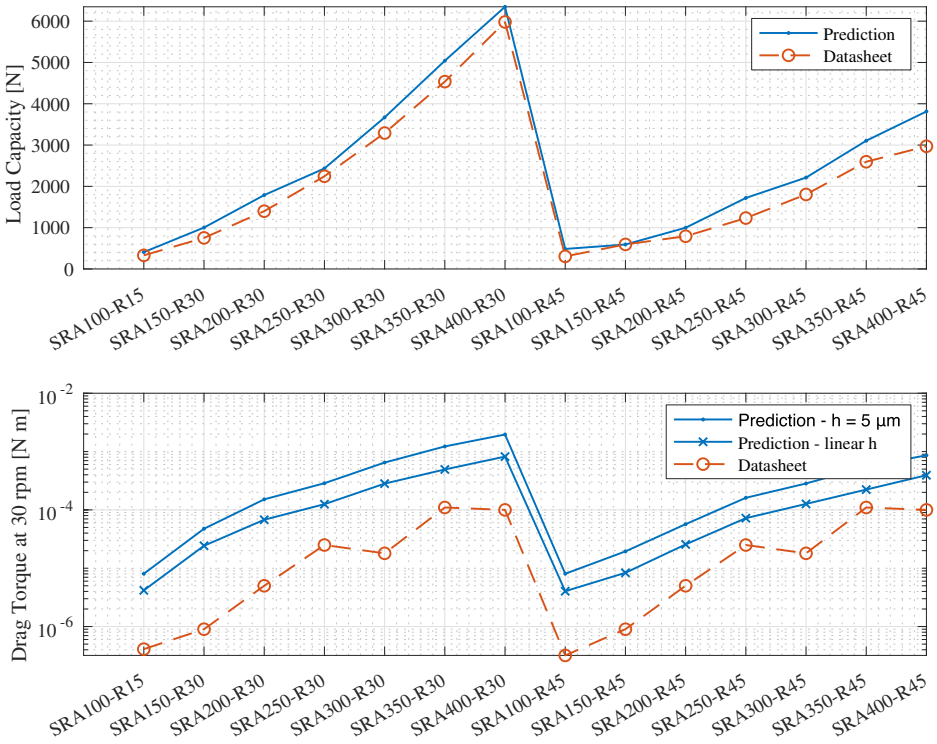

Fig. 7 Prediction of load capacity and drag torque for the Specialty Components SRA spherical air-bearing product line. Notice the logarithmic scale for the second plot.

The prediction of the load capacity is in accordance with the producer datasheets (with an average relative error of 24%). While this could seem a large error, we should consider that the limited knowledge of the geometry parameter and the assumption of linearly evolving pressure within the socket do not allow for a more torough analysis. Indeed, as shown in [23], the actual output pressure acting on the sphere at the inlet is, in general, lower than the total pressure. This justifies the higher values of the predicted values. Moreover, there are no information on the measurement conditions from the producer; this is a significant limitation because does not allow to define unambiguously wether a set of effects – including the external action of the air on the spherical slice exposed to the ambient pressure, or the weight of the sphere itself – are to be considered or not in the estimation. In general, as the trend of the predicted values matches the one of the datasheet, we consider the model for the load capacity to be a good first-order guess.

On the contrary, the prediction on the drag torque are completely different – by orders of magnitude – with respect to the one provided by the manufacturer. While the trend is actually coherent, every data point differs from the expected value of more than one order of magnitude (average ratio: 19.63). We noted that:

- the considered model did not even account for the drag on the exposed spherical surface, as the gradients within the gap have been considered higher;
- the data reported by the manufacturer for bearings of same radius are identical, even when the spherical area in the socket differed. The data for the SRA800-R45 is missing.
- The entire socket surface has been assumed equal to the viscous area of eq. (17). However, by observing the SRA250-R30 available at DART lab, the presence of a recess area on the bottom of the sphere and a series of grooves to guide the air outside the socket is evident, and probably correspond to areas in which the velocity gradients are much smaller.
- the considered gap height, in our analysis, has been assumed coherent to the one reported in the datasheet. However, as the tests have been performed with only the sphere loaded, one should expect a higher gap height, resulting in lighter gradients and a reduced value for the viscous force. In this regards, we performed the same analysis assuming the declared gap height (constant at 5 μm) as a baseline, and the actual gap height linearly varying with the applied load (as a spring). This halved the average ratio to about 9; still, there is a full order of magnitude of error.

- Additional effects – most notably, the turbine torque [26] that counteracts the drag effects – are captured by experimental setups, but do not find space in simplified models.

In order to investigate the disagreement between the manufacturer data and our calculation, we reached out by contacting the supplier. The answer confirmed our initial conjecture: the drag measurements were conducted with an unloaded sphere; therefore, the gap height was higher than the one assumed in our analysis, leading to lower shear actions on the interface. However, assuming a linear variation of the gap height with the applied load with rate equal to the provided stiffness, the prediction are still off. This suggests that a linear model for the gap height with the provided stiffness value is not a good approximation.

The provided analysis showed that both analytical models and producer datasheet information have to be taken cautiosly. Indeed, while simple models are not suitable with more complex geometry, literature suggests that both the load capacity and drag torque are variable quantities, whose trends are usually not reported on product datasheets. As experimental setups are difficult to achieve – due to the fact that multiple load conditions should be simulated, introducing additional drag effects due to interaction of the loads (and, in some cases, the measuring setup itself) with the surrounding air, the suggestion is to pursue other strategies – including the one of estimating the overall drag force acting on a specific platform through alternative methodologies illustrated in section II.B.2.

2. External air interaction

While the quantification of the air drag withing the sphere-socket interface can rely on simple, first-order model in order to obtain a ballpark figure – or, ultimately, higher-end models that take into account additional effects as the fluid flow at the socket entrance, the same cannot be done for the external air interaction effect. Indeed, each platform is different from the other and, therefore, such effects should be properly assessed through experimentation or numerical simulations. Simplifying models can be thought of. A topological decomposition can be performed according to the shape of the platform. In the following, an example of such topological decomposition:

$$\boxed{\text{Dumbbell configuration}} = 2 \cdot \boxed{\text{Flat plate friction force on appendices}} + 2 \cdot \boxed{\text{Drag of roto-translating cylinder}} + \boxed{\text{Drag torque over rotating sphere}}$$

$$\boxed{\text{Tabletop configuration}} = \boxed{\text{Flat plate friction force on top plate}} + N \cdot \boxed{\text{Drag of roto-translating cylinder}}$$

$$\boxed{\text{Hollow configuration}} = \frac{\theta_s}{\pi} \cdot \boxed{\text{Drag torque over rotating sphere}}$$

It should be noted that such an approach is simplistic and should not be trusted when high accuracy values are desired. However, when ballpark figures are needed, such approach can be useful to obtain a first-order estimation of the drag torque. In the following, we reported some empirical relationships for the drag torque for different fundamental geometries composing the three platform topologies identified.

For a rotating disk in a steady flow, [27] gives the following formula:

$$T_{\text{drag}} = 1.94 R^4 \rho \sqrt{\mu \omega^3} \tag{18}$$

T_{drag} = drag torque [N m]
ρ = air density [kg m^{-3}]
μ = air viscosity [N s m^{-1}]
ω = rotational velocity [rad s^{-1}]

For a rectangular flat plate in a free stream, the following formula can be used from Blasius solution (single-side):

$$dF_{\text{drag}} = \frac{0.664}{\sqrt{2\text{Re}_x}} \rho \mu v^2 c \, dx \tag{19}$$

dF_{drag} = infinitesimal drag force [N]
Re_x = local Reynolds number [·]
ρ = air density [kg m^{-3}]
μ = air viscosity [N s m^{-1}]
v = flat plate velocity [m s^{-1}]
c = coordinate orthogonal to flow field [m]
x = coordinate parallel to flow field [m]

The above formula should be integrated according to the flat plate shape. In case of a rectangular plate, if one

neglects the effect of the free edge, the above is in accordance with [28]:

$$T_{\text{drag}} = \frac{1.328}{2\sqrt{\text{Re}_l}} \rho \mu \omega^2 d^3 A \qquad (20)$$

T_{drag} = drag torque [N m]
Re_l = Reynolds number relative to parallel direction dimension [·]
ρ = air density [kg m^{-3}]
μ = air viscosity [N s m^{-1}]
ω = rotational velocity [rad s^{-1}]
d = distance of the plate from the center of rotation [m]
A = flat plate area [m^2]

For what concerns the torque of a rotating sphere in a steady flow, one can refer to Howarth's theory [29]:

$$T_{\text{drag}} = 2.93\sqrt{\mu\rho} R^4 \sqrt{\omega^3} \qquad (21)$$

T_{drag} = drag torque [N m]
μ = air viscosity [N s m^{-1}]
ρ = air density [kg m^{-3}]
R = sphere radius [m]
ω = rotational velocity [rad s^{-1}]

Finally, [ref] provides a sequence of drag coefficients for cylinders with different sections. By assuming the drag coefficient to be equal at any section, for a roto-translating cylinder the non-frictional drag can be written as:

$$T_{\text{drag}} = \frac{(d_0 + l)^4 - d_0^4}{4} c_d \rho \omega^2 R \qquad (22)$$

T_{drag} = drag torque [N m]
μ = air viscosity [N s m^{-1}]
ρ = air density [kg m^{-3}]
c_d = drag coefficient []
R = cylinder radius [m]
d = distance of the closest cylinder face from C.R. [m]
l = length of cylinder [m]

The above can be demonstrated by considerng a small axial section of the cylinder and integrating the infinitesimal drag torque over the length.

In order to check wether such lumped approach can give consistent results, we performed a Computational Fluid Dynamics (CFD) simulation taking the CAD model of STASIS as a reference. In particular, for the lumped approach the platform has been naively model as a set of flat plates (the one composing the solar panel, the main plate, the bottom one) and four rotating cylinders. Using the above formulas, the calculation resulted in an estimated drag coefficient equal to $9,97$e-6 Nm for a 1 rpm rotation condition over the vertical axis. This has been compared with a more complete CFD analysis carried on with the ANSYS Fluent simulation software. The steady-state solution was computed using the governing equation expressed in a rotating reference frame. In total, the resulting aerodynamic drag torque for a 1 rpm angular velocity equal to $2.63 \cdot 10^{-4}$ Nm.

As the effect of the rotating cylinders in the lumped approach was negligible (2.80e-11), the drag torque due to frictional forces only was extracted from the CFD solution ($2.73e-5$). While the lumped model was comparable in terms of order of magnitude, it underestimated the effect of frictional torques. More significant, however, is the fact that the non-frictional drag torques accounted for the most part of the total drag torque (about 90%). By looking at the torque distribution over the z-axis (**Figure** 8), indeed, a series of regions with high drag torque concentration were found due to fluid stagnation on the stiffening elements of the main plates and the presence of the moving masses, whose face normal is orthogonal to the velocity direction for a z-axis rotation.

Therefore, it was concluded that the estimation of the drag torque acting on the platform cannot rely on simple lumped models even for simplified geometries. The real platform topology leads to additional resistive torques due to the pressure distribution over the platform. Future works are planned to assess more toroughly the effects of such forces, in the attemp to build a predictive model that could be used for on-line compensation of the resulting torques.

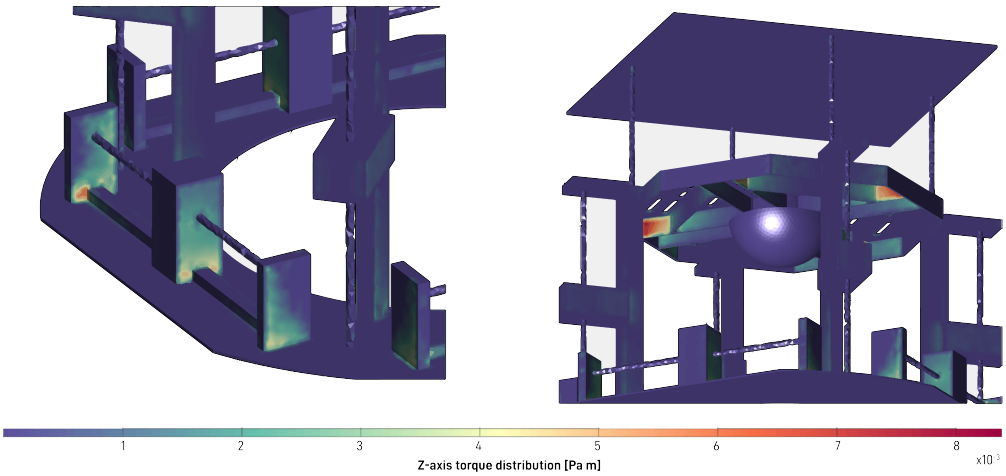

Fig. 8 Concentration of pressure torques on STASIS' external surfaces

C. Other sources of disturbances

Finally, the effect of other minor disturbance sources is assessed. In particular, the following are considered and discusses:

- magnetic-induced disturbances from Earth's magnetic field
- radiation pressure
- battery discharge

1. Magnetic-induced disturbances

The physical elements resulting in magnetic-induced disturbances are, of course, mostly due to Earth magnetic field. Again, the disclaimer made before starting the discussion on disturbances applies; indeed, the magnetic field disturbance is felt even for satellites on near-Earth orbits. The current most-accredited model for the magnetic field is given in [30], and consists on the gradient of a potential function:

$$V(r,\phi,\theta,t) = a\sum_{n=1}^{N}\sum_{m=0}^{n}\left(\frac{a}{r}\right)^{n+1}\left(g_n^m(t)\cos m\phi + h_n^m(t)\sin m\phi\right)P_n^m(\cos\theta) \tag{23}$$

Quantitatively speaking, the averaged value of the Earth magnetic field at the equator is:

$$B_0 = 3.12\cdot 10^{-5}\ \mathrm{T} \tag{24}$$

and, according to a simplified dipole model, varies with the colatitude θ calculated with respect to the magnetic north pole as:

$$|B| = B_0\left(\frac{R_\oplus}{r}\right)^3\sqrt{1+3\cos^3\theta} \tag{25}$$

Apart from the magnitufe and distance effect, the fundamental difference between space missions and an air-bearing platform lies in the time evolution of the magnetic field. Indeed, as spacecraft move around in space, the magnetic field vector experienced change, while it is constant on Earth on the timescales associated to the simulations. For this reason, and in order to enable higher simulation fidelity for any kind of orbits, magnetic-field-generating devices such as Helmoltz cages have traditionally been associated with the employment of air-bearing platforms [1, 2, 11]. The principle behind the Helmoltz cage is the generation of three orthogonal current loops in order to tune the magnitude and direction of the magnetic field within the cage. Two use cases can be distinguished:

- employment of Helmoltz cages to eliminate Earth's magnetic field [5];
- employment of Helmoltz cages to simulate a time-varying magnetic field [1, 2, 11**?**]

In the former case, the electrical and geometrical characteristics of the platform do not influence the simulation anymore (apart from any magnetic field generated by the platform itself). In the latter case, the electro-magnetic characteristic of the platform should be assessed in order to give coherent results in terms of perturbing torque with respect to the operating environment. Moreover, as not every setup provides a Helmoltz cage, a set of considerations should be made for this application too. In order to quantify the effect of magnetic disturbances due to Earth's magnetic field, one should first introduce the model for the magnetic perturbing torque. The concept of magnetic moment $\vec{m}$ is introduced. For a body in an external magnetic field $\vec{B}$, the resulting magnetic torque acting on the body can be expressed as the cross product of its magnetic moment and the magnetic field vector:

$$\vec{T}_{\text{mag}} = \vec{m} \times \vec{B} \tag{26}$$

For non-ferromagnetic materials, the computation of the magnetic dipole moment can be performed by knowing the current distribution on the object itself, according to the formula:

$$\vec{m} = \frac{1}{2} \iiint_V \vec{r} \times \vec{j} dV \tag{27}$$

Of course, it would be presumptious to be able to know all the localized current distribution on the air-bearing platform. However, by knowing the platform design, one should be able to identify a series of current loops on the platform, reducing the integral above to:

$$\vec{m} = \sum_{i=1}^{N_{\text{loop}}} I_i \vec{S}_i \tag{28}$$

with $\vec{S}_i$ being the oriented area vector related to the i-th current loop. Note that the resulting expression is not dependent on the location of the current loop with respect to the CoR of the platform, just on their overall area.

For the dumbbell-style platform, the effect of the magnetic disturbance torque, assuming a configuration with current loops around the entire instrumentated plate, is a torque around the vertical axis that tends to align the platform to the magnetic field (**Figure** 9a). In this sense, the platform acts as a compass. In the case of the tabletop configuration, instead, assuming a full current loop over the main plate, the effect is to tilt the platform aligning the main plate with the magnetic field. In this case, there is both an effect of rotation and a tilt effect (**Figure** 9b).

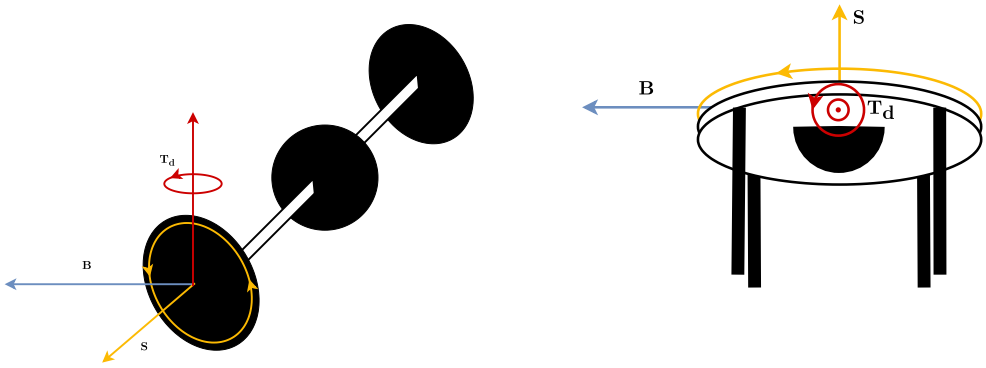

(a) Dumbbell **(b) Tabletop**

Fig. 9 Effect of magnetic disturbance on different configurations

2. Radiation pressure

It comes fairly natural to think of space-based Solar Radiation Pressure (SRP) when discussing the disturbances arising up due to the platform irradiation by natural and/or artificial sources of light. State-of-the-art models for the SRP result, for typical spacecrafts, SRP force values between 10^{-9} and 10^{-8} N. When the pressure distribution is not symmetrical, this translates in a torque according to the geometry of the satellite. Regarding air-bearing platform, it is convenient to distinguish between natural light effects and beaming devices. The latter can include solar simulators

[1, 31] or power-beaming devices [6] for power generation. We state with confidence that the effect of the former can safely be neglected compared to other sources of disturbances. Indeed, values of indoor light irradiance range between 0 and 100 W/m^2, between one and two orders of magnitude less than the one felt in the space environment [32]. Moreover, all thre three typologies of platforms here considered have a fairly simmetric structure that naturally eliminates the toruqes arising from the pressure radiation distribution on the body. On the contrary, the effect of power-beaming devices should not be neglected. Solar simulator share, by definition, the same spectral and radiation pattern characteristics of the Sun. These include an irradiance value in the order of 1000 W/m^2 (according to the mission to be simulated) and a collimated beam. The beam collimation results in uniform distribution over the platform; however, platform asymmetries and self-shadowing effects (notoriously difficult to quantify) should be taken into account. Moreover, perfect collimation is difficultly achievable. In section III.B, it is shown how the STASIS power beaming system achieves non-uniform illumination on the solar array due to a beam divergence angle of 3 deg. Together with a limited footprint of the beam, it is not straightfoward to directly estimate the resulting torque. In order to give a quantitative figure, a ray-tracing approach – similar to the one described in section III.B – was employed to calculate the net force distribution on the top plate. Neglecting the effect of External Quantum Efficiency (EQE) and assuming all the radiation absorbed by the solar array, the employed formula for the force acting on a single area element was calculated as:

$$\Delta\vec{F} = -\frac{I(\vec{r})}{c}\Delta A(\hat{\vec{I}}\cdot\hat{\vec{n}}_A)\hat{\vec{I}} \qquad (29)$$

$\Delta\vec{F}$ = force due to radiation pressure [N]
$I(\vec{r})$ = irradiance at the area centroid [W/m^2]
ΔA = element area [m^2]
$\hat{\vec{n}}_A$ = element area normal [·]
$\hat{\vec{I}}$ = radiation direction [·]

The radiation intensity and direction were easy to obtain exploiting the ray-tracing approach; indeed, the whole light source was divided in a set of rays carrying the same amount of energy. Subsequently, the entire area was binned in a 100x100 matrix of ΔA elements, and element-wise operations were performed to compute the net force $\Delta\vec{F}$ and, subsequently, the net torque due to radiation pressure with respect to the geometrical center of rotation (**Figure** 10).

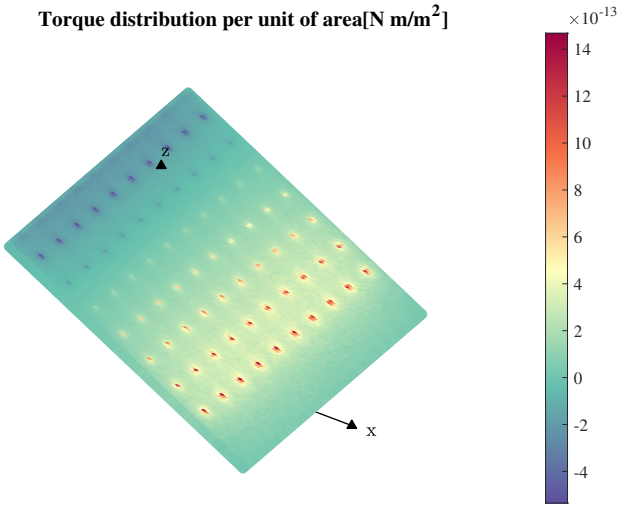

Fig. 10 y-component of the torque distribution acting on the platform. The x and z components have not been displayed because the former was auto-balanced in the selected geometry configuration and the second one was negligible due to the low beam divergence angle.

The result was a net torque around the y-axis equal to $1.127 \cdot 10^{-9}$ Nm. Considering that, despite this value being comparable to the one of a real spacecraft mission, the figure is order of magnitudes lower with respect to other sources of perturbation and that it is an instantaneous value calculated with the platform at the limit angle of 30 deg, it is considered safe to neglect the effect of pressure radiation even in the case of high-power beams directly impinging on the platform.

3. Battery discharge

In the original NASA document [5], the effect of battery discharge on the CoM shift was mentioned. Notably, it was one of the issues for which no satisfactory solution was identified. In recent works, the issue is never raised up. In this work, we are interested to understand wether the assumption of negligible CoM shift due to battery discharge is generally applicable. It should be noted that even outside the aerospace literature, no prior work investigating such an effect has been found. Nonetheless, it is possible to derive a simple model for the CoM shift of Li-ion batteries by making some assumption on common state-of-the-art commercially-available single-cell batteries. The process governing the CoM shift is the displacement of the lithium ions within the battery. Indeed, the process of current generation is due to the fact that the lithium atoms originally located in the anode lose an electron due to the voltage difference. The resulting Li^+ ion is attracted by the cathode, crossing the separator and forming a new chemical bound with the cathode atoms. The relocation of the Li-ion atoms eventually results in the mass shift from the charged and discharged state (**Figure** 11).

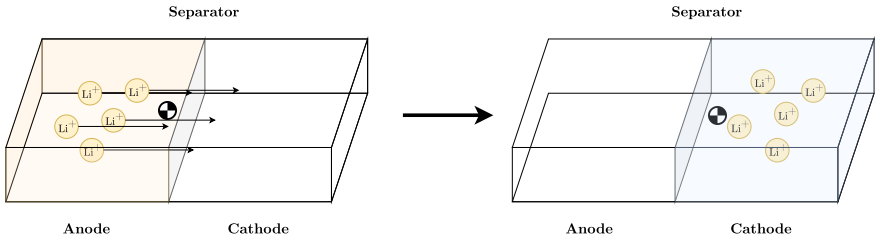

Fig. 11 Illustration of the CoM shift due to battery discharging. The lithium ions cross the separator and bond themself to the cathode, changing the mass distribution of the battery

The quantification of the mass shift requires the knowledge of the internal battery geometry, the chemical reactions involved in the discharging process, and the quantity of moving atoms in the battery. These ultimately can vary according to both the battery chemistry, the battery design, and the manufacturing process. In the case of a battery of a lithium-doped cobalt oxide cathode and a graphite anode, the reactions governing the discharging process are the following [33]:

$$\mathrm{LiC_6} \longrightarrow \mathrm{C_6} + \mathrm{Li^+} + \mathrm{e^-}$$
$$\mathrm{Li^+} + \mathrm{e^-} + \mathrm{CoO_2} \longrightarrow \mathrm{LiCoO_2}$$

Therefore, assuming complete discharging, all the Li ions are shifted from the anode to the cathode. Under such assumption, a formula to estimate the CoM shift due to battery discharge is:

$$\Delta\vec{r}_{CM,depl} = \frac{m_{Li}\vec{r}_{AC}}{m_{tot}} \qquad (30)$$

$\Delta\vec{r}_{CM,discharge}$	=	CoM shift due to battery discharge [m]
m_{Li}	=	mass of lithium as found in the battery [kg]
$\vec{r}_{AC}$	=	anode-cathode position vector [m]
m_{tot}	=	overall platform mass [kg]

The above equation can be specialized according to generic type of battery chemistries. For generic Li-ion batteries, an expression to related the mass content of Lithium with respect to the battery capacity in Ah can be calculated by rounding the energy delivered by the umber of Li atoms in a gram of lithium (each atom releases 1 electron):

$$m_{Li}[\mathrm{g}] = 0.3 \cdot C[\mathrm{A_h}] \qquad (31)$$

specializing eq. (30) in:

$$\Delta\vec{r}_{CM,\mathrm{depl}} = \frac{0.0003C\vec{r}_{AC}}{m_{\mathrm{tot}}} \qquad (32)$$

By applying the above formula to some commercially available Li-ion batteries, a rough estimate of the CoM can be given. In STASIS, the employed batteries are the VARTA EasyPack XL. These are characterized by a total capacity of 2400 mAh and a maximum dimension of about $64mm$. Assuming the cathode and anode regions separated along the

higher dimension, and assuming the Li-ions uniformly distributed across the length of the battery, the resulting CoM shift between the fully-charged and fully-discharged conditions is – considering a platform of 7 kg – of about:

$$|\Delta\vec{r}_{CM,\text{depl}}| = \frac{0.0003C|\vec{r}_{AC}|}{m_{tot}} = \tag{33}$$

$$= \frac{0.0003 \cdot 2.4 \cdot 0.03225}{7} = 3.32 \cdot 10^{-6} \text{ m} \tag{34}$$

The above figure corresponds to a perturbation torque due to Earth's gravity equal to about $2.3 \cdot 10^{-4}$ Nm. This value is comparable to the drag torque computed in section II.B.2. Moreover, it should be considered that the above figure is for a single battery of small capacity. Indeed, it would allow simulating a 2 A, 3.7 V instrumentation for a little more than one hour. Power-hungry devices, such as reaction wheels or motors, operating at higher voltages, would require bigger batteries for continuous operations – expecially in longer experiments. In order to mitigate the problem, a single solution would be employing identical batteries arranged in a symmetric configuration. This way, assuming uniform discharging through series or parallel connection, the resulting CoM shift would be nullified. Still, the CoM shift would have an effect also in terms of the inertia matrix; however, it should be noted that inertia changes due to battery discharging are a phenomena that is present even in real satellites and, therefore, the inclusion of the latter effect in the simulation could be beneficial in terms of faithfulness.

III. Operability in real-time hardware-the-loop simulations

Attitude simulation platform are widely employed in hardware-in-the-loop simulations. The possibility to host multiple devices and instruments potentially makes them a precioous and flexible testbed that can be adapted for a multitude of purposes. However, their characteristic also bring a set of limitations that should be properly taken into accound when designing HiL experiments. In particular, we will focus on the employment of such platforms in real-time integrated simulations, in which the on-platform systems must interface with other components. In particular, the following aspects will be investigated:

A) the ability to retrieve the actual orientation of the platform and to map to the one of a spacecraft;
B) the constraints of having an untethered platform in terms of power supply;
C) the challenges associated to the integration of wireless communications in a real-time simulation environment.

A. Attitude estimation techniques

When employing the air-bearing platform as a tool for attitude systems and algorithms, it is paramount not only to ensure that the platform is actually able to simulate the atittude evolutino of a real spacecraft, but also to be able to retrieve performances measures associated to the object of the testing campaing. This measure is often associated to the actual orientation and/or angular velocity of the platform. Therefore, it is critical to employ a system to retrieve such information accurately. When discussing on the accuracy of the system, one should reason on the system/algorithm expectations and requirements. This means that the capability of the platform attitude estimation system should be at least on-par with the acceptable error on the performances of the system to be tested. In general, at least an additional order of magnitude of accuracy is required [34]. It would have little sense to test an attitude control algorithm with sub-arcsecond precision with an attitude estimation technique that is only accurate at 1 deg. Nonetheless, attitude estimation systems and techniques are not trivial and usually cumbersome to implement. On the other side, as the platform is operated on ground, it is possible to employ attitude estimation systems not typically available in space application, including optical or radiometric devices, tracking algorithms, encoders, and additional environmental references (such as Earth magnetic field).

In general, apart from the accuracy requirement, another fundamental criticality consists in the *validation* of such a measuring device. It is clear that, in order to guarantee accuracy of the measuring system up to a desired error, the reference measures used for validation should be known – again – at least at one order of magnitude of precision. This is a well-known problem in metrology (who validates the ground truth?). The current trend in the case of air-bearing platform is to employ third-party reference systems which accuracy is stated by the manufacturer on the device datasheet. While this may seem a convenient shortcut to get rid of the ground truth problem, it should be noted that such information are usually reductive and safety margins in the fidelity of the measurement should be taken due to the operative and environmental conditions being different from the ones used in the device validation.

Regarding attitude estimation, the technologies we are going to cover are reported in the following. The list is not to be considered exhaustive, but:

- MEMS inertial units, such as IMUs and gyros;
- encoders;
- camera-based systems

The main issue associated with electronic devices for attitude measuring is in terms of performance. Commercially-available MEMS gyroscope typically offer accuracy levels in the order of hundreds of arcsecs; moreover, they are easily subjected to bias drift phenomena that hinder their employment in long-term simulations. This suggest that raw gyroscope data cannot be used as-is in the context of attitude estimation, but attitude estimation filters – using sensor fusion algorithms – should be foreseen. However, in the context of high-accuracy attitude estimation, alternatives such as tactical-grade or navigation-grade inertial measuring units should be employed. Still, even high-performance devices are subjected to bias instability and, therefore, should be run in conjuction with attitude estimation technique. In this regard, it should be noted that most algorithms necessitate a reference dynamic model and a set of physical parameters (such as the inertia tensor); the dynamic model should be augmented to include all the disturbances introduced before, while the estimation of the physical parameters is often dependent on the observation of the dynamics itself [35] – and therefore depend on the accuracy of the measurement itself.

Encoders do not suffer, in theory, from the divergence of the measure from the real value over time. The position of a magnetized device is sensed by a set of magnetic sensor; through the knowledge of the magnetic field and the interpolation of the sensor readings it is possible to reconstruct the angular position of the target (in this case, the spherical interface). High-end rotary encoders can reach accuracies in the order of 100,000s of counts per rotation (arcsecs), while inductive ones can reach millions of cpr. *. However, to our knowledge, air-bearing setups with rotary encoders are only available in cylindrical configuration, due to the difficulty of implementing a three-dimensional device able to reconstruct the attitude over multiple axes, making the technology not feasible in the case of spherical air-bearings.

Camera-based systems work by taking one or multiple snapshots of the platform and inferring its orientation exploiting the a-priori knowledge of their geometrical configuration. Usually, the platform should be augmented with a set of trackers or markers to ease the attitude estimation system process. Among these, checkerboard patterns [1], reflective markers [36], or radiation-emitting devices (such as LEDs) [37]. The accuracy level vary on the camera resolution and the characteristic dimension of the markers, but can reach accuracies of a few arcsecs. STASIS mounts in-house-built LED-based attitude tracking system consisting in a LED board – manufactured at high tolerance, and assembled with 0201-packaged LED devices – and a monocular camera, capable of performing attitude estimation up to 12 arcsecs of precision for in-plane rotation and 37 arcsecs for out-of-plane at 160 Hz [37]. Another advantage of camera-based system, differently from the previous categories, is the possibility to run the attitude estimation algorithms off-board. This removes all the latencies characterizing wireless transmission and allows the deployment of the attitude measuring system in real-time.

B. Power supply

One of the main issues to consider is the limited availability of onboard power storage. Indeed, current battery technology would allow a limited timespan for a simulation, restricting the applicability to a limited set of maneuvers and conditions. Moreover, heavily discharging batteries can hinder the simulation faithfulness as some of the commonly employed battery chemistries result in the batteries' center of mass changing with the state of charge, as noticed before in [5] and discussed in section II.C.3. In the context of integrated simulation, even assumping active compensation of the CoG shift due to battery discharge, the power requirements of the platform are a limiting factor in the execution of long-lasting experiments. Assuming a nominal consumption of all the on-board instrumentation of 25 W, indeed, state-of-the-art battery technologies would require 360 Wh for a 24-hours experiment, requiring about 2,5 – 6 kg of Li-ion batteries. In the context of interplanetary transfers, with charactristic mission times of months, if not years, even an accelerated simulation is expected to last multiple days, leading to the power supply being the bottleneck restricting the employment of such platforms to isolated mission phases and maneuvers. As charging cables are a clear no-go, wireless power transmission technologies could free air-bearing platforms from such constraints. In particular, we are going to discuss the following technologies:

- microwave power transmission systems, employing rectennas on top of the platform;
- inductive power generation system, with coils underneath the ball-socket interface;

*Source: `https://www.celeramotion.com/zettlex/high-resolution-encoder/`

• power beaming solutions, with photovoltaic devices on board and a power beamer outside.

With respect to microwave power transmission system, it could be possible to achieve high values of conversion efficiecies (up to 90% for 2.45 GHz transmission frequency and 82% for 5.8 GHz [38]). Rectenna are a clever solution and are capable of achieving almost unitary power transmission efficiency. They can be printed and designed in many shapes [39, 40], and operate in a radiation spectrum that is relatively safe for humans. A possible issue is related to possible interferences with wireless communication signals (as most WiFi transmission also happen in the same spectral range), but this issue can be circumvented by operating the same at different frequencies. The main limitation, in our opinion, is their procurement and manufacturing. Indeed, off-the-shelf components are either difficult to obtain, or expensive compared to other lab instrumentation. Finally, the attitude motion of the platform could result in efficiency losses according to the employed radiation patterns of the emitter and receiver.

Inductive power generation systems, on the contrary, do not require expensive setups and/or devices, are easy to manufacture or procure, and do not require antenna pointing. However, they also suffer from efficiency losses due to the platform motion. Indeed, they are mostly efficient when the coupled coils are parallel [41]. Nonetheless, the main limitation associated to such kind of systems is the effect of the resulting magnetic field. Indeed, the working mechanism lies in the generation of a magnetic field from the first coil, inducing a current in the receiver coil. According to what discussed in section II.C.1, this could lead to disturbance torques affecting the fidelity of the simulation. However, with proper setup and analysis, it should be possible to minimize and quantify such effects, employing compensation techniques to circumvent the issue.

Finally, power beaming systems work by employing a power beaming device – such as a high-power lamp – irradiating a photovoltaic received. Differently from rectennas, that employ rectification to convert the input energy into DC current, photovoltaic devices exploit photovoltaic effect to generate a current. Among the considered devices, power beaming devices are the least complex from a procurement/manufacturing point of view. Indeed, emitters (such as LED diodes), optics, and receives (mostly solar cells) are easy to find as off-the-shelf components. While traditional datasheet efficiencies for Si-based solar cells vary between 15 – 25%, by properly tuning the emission source higher efficiencies can be achieved. In [42], a 68.9% efficiency has been achieved with a power beaming system. Lower values around 30 – 40% have been repeatedly obtained in lab environments [43, 44]. The design of STASIS foresee a solar array capable of reaching a source-to-cell illumination efficiency of about 90%, employing high-power LEDs with tailored ultra-narrow-beam collimating optics, and a conversion efficiency of about 38% by using LEDs in the far red range (730±15 nm). The expected continuous power output in nominal conditions is of about 30 W (**Figure** 12). When inclined at 30 deg, the maximum theoretical expected power output is of 23 W; however, the non-uniform illumination results in lower power output due to the difficulty in tracking the maximum power point.

C. Wireless communication

When employing air-bearing platform in integrated hardware-in-the-loop experiments, two situations can arise. The first is characterized by the on-board employment of all the devices involved in the simulation, including all the sensors, actuators, and computing units. This condition – assuming a proper cable management strategy, that does not result in time-varying inertial parameters within the simulation – has as only limitation the one related to the power supply discussed before in section III.B. When employing the platforms in tandem with external devices and units, instead, a series of problems related to the communication between the on-board instrumentation and the devices external to the platform arise. These problems are further amplified under the requirement of a real-time simulation. The locution *real-time simulation* refers to a particular kind of computational simulation in which the simulation step-time is synchronized with the real-world step [45]. As a consequence, real-time simulation require all the operations to be carried on in a single time-step to be actually computed in a timeframe that is shorter than the employed time-step, in order to be able to perform any additional simulation management activity and carry on to the next step, keeping the simulation clock and the real-world clock always synchronized. The clock synchornization requirement automatically imposes a hard time constraint on all computing activities to be performed within the simulation, bringing in all the discussion on real-time computing. *Real-time computing* refers to a branch of numerical computing in which the correctness of an operation is not only given by the result of an operation itself, but also on the time required for it to complete [46]. Despite commonly associated to fast computing, real-time computing does not necessarily require all the operations to be exectued at high throughput, just that they shall complete before a hard time limit. When the operations involve communication between two or more devices, we speak of *real-time communication*. In order to guarantee real-time communication, over the years a series of real-time communication protocols have been developed [47, 48]. However, the current panorama still lacks a widespread implementation of a wireless real-time communication protocol.

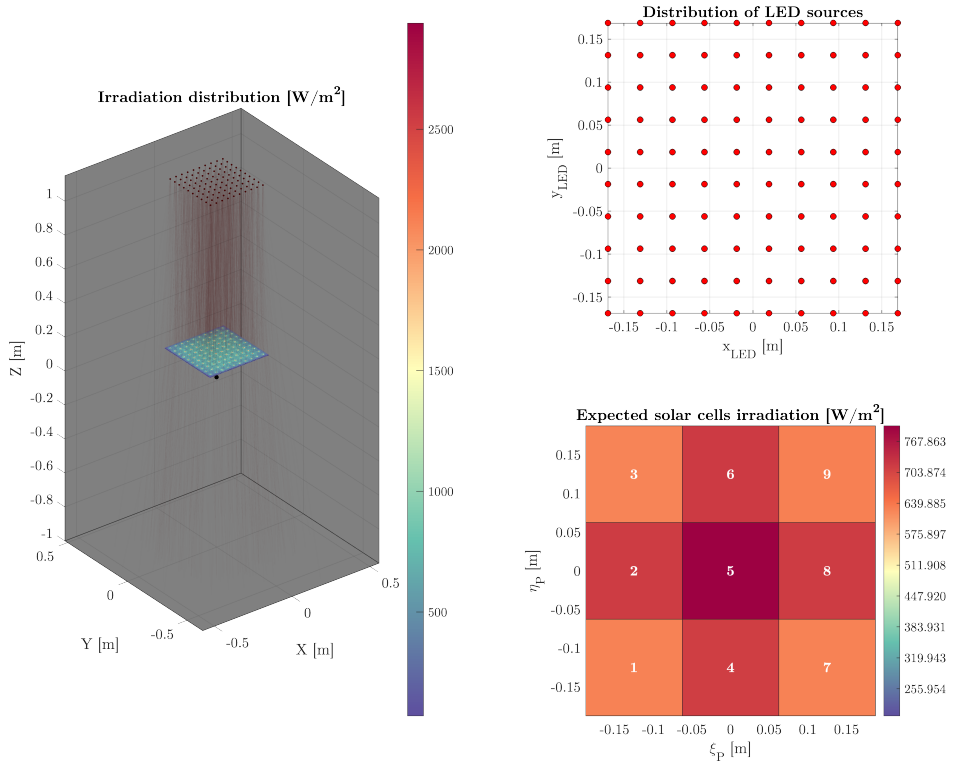

Fig. 12 Simulation outputs for the ray-tracing analysis of STASIS' power beaming solution, for two different platform orientations [6].

Indeed, traditional wireless applications – including Wi-Fi, Bluetooth, ZigBee, and others – have no guarantees nor checks on the time required for packet delivery due to the aleatorieties associated to distance, interference, obstacles, access points, and switching, routing, and bridging devices. The most promising framework for a seamless integration of traditional IP wireless communication in a real-time framework are the RT-WiFi framework [49] and the UDP-RT[†] framework. Both are based on the 802.11 PHY interface typically used in common wireless LAN networks. However, to our knowledge, there is currently no standard for real-time wireless communication. This is because a flexible setup of the network infrastructure is often preferred in order to accomodate dynamic requests of multiple agents and device. Currently, no out-of-the-box solution exists to our knowledge, and the implementation, verification, and validation of the real-timeness of the communication infrastructure is left to the experiment operators and designers.

Conclusions

In this work, a qualitative and quantitative study on the sources of disturbances affecting attitude simulation platform based on air-bearing sphearical joints has been performed. Before proceeding with the analysis, the definition of disturbance has been given, and caution was suggested in order to determine which effects to assume as such and, conversely, which ones can be left acting on the platform without affecting the experiment faithfulness and validity. The structural and aerodynamic aspects, assumed to be the dominant ones, have been dissected and a set of analytical relations has been given in order to quantify the effect of resulting disturbance torques. It has been shown that, according to the topology of the platform, such relations can differ and are usually attitude-dependent; in light of this, it is not possible to compensate such effects by acting directly on the platform configuration. When analyzing other sources of disturbances, the effect of magnetic torques, radiation pressure, and battery discharge have been assessed. Further works will also give a treatment of the effects due to gravity gradient – a phenomenon that affects also satellites orbiting close to the Earth – and seismic effects. Eventually, a series of discussion on the operability of such platforms in integrated, real-time, hardware-in-the-loop experiments has been discussed, focusing on the issues related to the wireless-ness of

[†]Source: `https://www.codeproject.com/Articles/275715/Real-time-communications-over-UDP-protocol-UDP-RT`

the platforms in terms of attitude estimation, power supply, and communication. Throughout all analysis and discussion, examples on the design solutions applied in the realization of STASIS, the EXTREMA attitude simulation platform, have been illustrated. Overall, it has been shown that a comprehensive model of an air-bearing platform can not neglect effects usually ignored in the literature (e.g., battery discharge) and that the operation of such platforms for prolonged experiments needs a careful assessment of the simulation infrastructure. Further works aim to complete the treatments hereby deferred, complementing the analytical relations with experimental data and measurements, and the proposal of a general-purpose simulation infrastructure for long-term operation fo the platform under minimal loss of faithfulness.

Acknowledgments

This project has received funding from the European Research Council (ERC) under the European Union's Horizon 2020 research and innovation programme (grant agreement No. 864697).

References

[1] Modenini, D., Bahu, A., Curzi, G., and Togni, A., "A dynamic testbed for nanosatellites attitude verification," *Aerospace*, Vol. 7, No. 3, 2020, p. 31. https://doi.org/10.3390/aerospace7030031.

[2] Chesi, S., Perez, O., and Romano, M., "A dynamic, hardware-in-the-loop, three-axis simulator of spacecraft attitude maneuvering with nanosatellite dimensions," *Journal of Small Satellites*, Vol. 4, No. 1, 2015, pp. 315–328.

[3] Jian, X., Gang, B., QinJun, Y., and Jun, L., "Design and development of a 5-DOF air-bearing spacecraft simulator," *2009 International Asia Conference on Informatics in Control, Automation and Robotics*, IEEE, 2009, pp. 126–130. https://doi.org/10.1109/CAR.2009.7.

[4] Schwartz, J. L., Peck, M. A., and Hall, C. D., "Historical review of air-bearing spacecraft simulators," *Journal of Guidance, Control, and Dynamics*, Vol. 26, No. 4, 2003, pp. 513–522. https://doi.org/10.2514/2.5085.

[5] Smith, G. A., "Dynamic simulators for test of space vehicle attitude control systems," *Proceedings of the Conference on the Role of Simulation in Space Technology, Part C, Virginia Polytechnic Inst. and State University, Blacksburg, VA*, 1965, pp. XV1–XV30.

[6] Di Domenico, G., Topputo, F., et al., "STASIS: an Attitude Testbed for Hardware-in-the-Loop Simulations of Autonomous Guidance, Navigation, and Control Systems," *73rd International Astronautical Congress (IAC 2022)*, 2022, pp. 1–20.

[7] Di Domenico, G., Andreis, E., Carlo Morelli, A., Merisio, G., Franzese, V., Giordano, C., Morselli, A., Panicucci, P., Ferrari, F., and Topputo, F., "The ERC-Funded EXTREMA Project: Achieving Self-Driving Interplanetary CubeSats," *Modeling and Optimization in Space Engineering: New Concepts and Approaches*, Springer, 2022, pp. 167–199. https://doi.org/10.1007/978-3-031-24812-2_6.

[8] Di Domenico, G., Andreis, E., Morelli, A. C., Merisio, G., Franzese, V., Giordano, C., Morselli, A., Panicucci, P., Ferrari, F., and Topputo, F., "Toward Self-Driving Interplanetary CubeSats: the ERC-Funded Project EXTREMA," 2021. Cited by: 6.

[9] Kim, J. J., and Agrawal, B. N., "Automatic mass balancing of air-bearing-based three-axis rotational spacecraft simulator," *Journal of Guidance, Control, and Dynamics*, Vol. 32, No. 3, 2009, pp. 1005–1017. https://doi.org/10.2514/1.34437.

[10] Prado, J., Bisiacchi, G., Reyes, L., Vicente, E., Contreras, F., Mesinas, M., and Juárez, A., "Three-axis air-bearing based platform for small satellite attitude determination and control simulation," *Journal of Applied Research and Technology*, Vol. 3, No. 3, 2005, pp. 222–237. https://doi.org/10.22201/icat.16656423.2005.3.03.563.

[11] da Silva, R. C., Borges, R. A., Battistini, S., and Cappelletti, C., "A review of balancing methods for satellite simulators," *Acta Astronautica*, Vol. 187, 2021, pp. 537–545. https://doi.org/10.1016/j.actaastro.2021.05.037.

[12] Chesi, S., Gong, Q., Pellegrini, V., Cristi, R., and Romano, M., "Automatic mass balancing of a spacecraft three-axis simulator: Analysis and experimentation," *Journal of Guidance, Control, and Dynamics*, Vol. 37, No. 1, 2014, pp. 197–206. https://doi.org/10.2514/1.60380.

[13] Bahu, A., and Modenini, D., "Automatic mass balancing system for a dynamic CubeSat attitude simulator: development and experimental validation," *CEAS Space Journal*, Vol. 12, No. 4, 2020, pp. 597–611. https://doi.org/10.1007/s12567-020-00309-5.

[14] Schwartz, J. L., and Hall, C. D., "Comparison of system identification techniques for a spherical air-bearing spacecraft simulator," *Advances in the Astronautical Sciences*, Vol. 116, 2004, pp. 1725–1741.

[15] Rahman, M. F., Poo, A., and Chang, C., "Approaches to design of ministepping step motor controllers and their accuracy considerations," *IEEE Transactions on Industrial Electronics*, , No. 3, 1985, pp. 229–233. https://doi.org/10.1109/TIE.1985.350163.

[16] Gao, Q., Chen, W., Lu, L., Huo, D., and Cheng, K., "Aerostatic bearings design and analysis with the application to precision engineering: State-of-the-art and future perspectives," *Tribology International*, Vol. 135, 2019, pp. 1–17. https://doi.org/10.1016/j.triboint.2019.02.020.

[17] Ezenekwe, D. E., and Lee, K.-M., "Design of air bearing system for fine motion application of multi-DOF spherical actuators," *1999 IEEE/ASME International Conference on Advanced Intelligent Mechatronics (Cat. No. 99TH8399)*, IEEE, 1999, pp. 812–818. https://doi.org/10.1109/AIM.1999.803277.

[18] Ezenekwe, D., and Lee, K.-M., "Design of air bearing system for fine motion application of multi-DOF spherical actuators," *1999 IEEE/ASME International Conference on Advanced Intelligent Mechatronics (Cat. No.99TH8399)*, 1999, pp. 812–818. https://doi.org/10.1109/AIM.1999.803277.

[19] Kothari, M., Booker, J., and Bartel, D., "Analysis of artificial hip joints as spherical bearings," *Tribology Series*, Vol. 30, Elsevier, 1995, pp. 93–98. https://doi.org/10.1016/S0167-8922(08)70620-5.

[20] Reynolds, O., "IV. On the theory of lubrication and its application to Mr. Beauchamp tower's experiments, including an experimental determination of the viscosity of olive oil," *Philosophical transactions of the Royal Society of London*, , No. 177, 1886, pp. 157–234.

[21] Meyer, D., "Reynolds Equation for Spherical Bearings ," *Journal of Tribology*, Vol. 125, No. 1, 2002, pp. 203–206. https://doi.org/10.1115/1.1506319.

[22] Childs, P. R., "Chapter 6 - Rotating Cylinders, Annuli, and Spheres," *Rotating Flow*, edited by P. R. Childs, Butterworth-Heinemann, Oxford, 2011, pp. 177–247. https://doi.org/10.1016/B978-0-12-382098-3.00006-8.

[23] Al-Bender, F., *Air bearings: theory, design and applications*, John Wiley & Sons, 2021.

[24] Elescandarany, A. W., "Analytical study of the spherical hydrostatic bearing dynamics through a unique technique," *Scientific Reports*, Vol. 13, No. 1, 2023, p. 19364. https://doi.org/10.1038/s41598-023-46296-5.

[25] Mahloul, M., Mahamdia, A., and Kristiawan, M., "Experimental investigations of the spherical Taylor-Couette flow," *Journal of Applied Fluid Mechanics*, Vol. 9, No. 1, 2016, pp. 131–137. https://doi.org/10.36884/JAFM.9.SI1.25828.

[26] Hsieh, J. H., Huang, J.-Y., Yen, T., Lee, S., Chang, A., and Hou, L., "Attitude Control Calibration and Experiment Testbed to Characterize Attitude Determination and Control System Performance," 2022.

[27] Cochran, W. G., "The flow due to a rotating disc," *Mathematical Proceedings of the Cambridge Philosophical Society*, Vol. 30, No. 3, 1934, p. 365–375. https://doi.org/10.1017/S0305004100012561.

[28] Stewartson, K., "On the flow near the trailing edge of a flat plate," *Proceedings of the Royal Society of London. Series A. Mathematical and Physical Sciences*, Vol. 306, No. 1486, 1968, pp. 275–290. https://doi.org/10.1098/rspa.1968.0150.

[29] Howarth, L., "CXXIX. Note on the boundary layer on a rotating sphere," *The London, Edinburgh, and Dublin Philosophical Magazine and Journal of Science*, Vol. 42, No. 334, 1951, pp. 1308–1315. https://doi.org/10.1080/14786444108561386.

[30] Thébault, E., Finlay, C. C., Beggan, C. D., Alken, P., Aubert, J., Barrois, O., Bertrand, F., Bondar, T., Boness, A., Brocco, L., et al., "International geomagnetic reference field: the 12th generation," *Earth, Planets and Space*, Vol. 67, 2015, pp. 1–19. https://doi.org/10.1186/s40623-015-0228-9.

[31] Kato, T., Heidecker, A., Dumke, M., and Theil, S., "Three-axis disturbance-free attitude control experiment platform: FACE," *Transactions of the Japan Society for Aeronautical and Space Sciences, Aerospace Technology Japan*, Vol. 12, No. ists29, 2014, pp. Td_1–Td_6.

[32] Apostolou, G., Reinders, A., and Verwaal, M., "Comparison of the indoor performance of 12 commercial PV products by a simple model," *Energy Science & Engineering*, Vol. 4, No. 1, 2016, pp. 69–85. https://doi.org/10.1002/ese3.110.

[33] Bergveld, H., "Battery management systems : design by modelling," *International Journal of Chemical Reactor Engineering*, 2001.

[34] Marvel, J. A., Falco, J., and Hong, T., "Ground truth for evaluating 6 degrees of freedom pose estimation systems," *Proceedings of the Workshop on Performance Metrics for Intelligent Systems*, 2012, pp. 69–74. https://doi.org/10.1145/2393091.2393106.

[35] Schwartz, J. L., and Hall, C. D., "System identification of a spherical air-bearing spacecraft simulator," *AAS Paper*, Vol. 122, 2004, pp. 8–12.

[36] Kolvenbach, H., and Voellmy, M., "Design of a Low-Cost, Spherical Air-Bearing Satellite Simulator," *Symposium on Advanced Space Technologies in Robotics and Automation (ASTRA)*, 2019.

[37] Ornati, F., Domenico, G. D., Panicucci, P., and Topputo, F., "High-accuracy Vision-Based Attitude Estimation System for Air-Bearing Spacecraft Simulators," , 2023. https://doi.org/10.48550/arXiv.2312.08146.

[38] McSpadden, J., Fan, L., and Chang, K., "Design and experiments of a high-conversion-efficiency 5.8-GHz rectenna," *IEEE Transactions on Microwave Theory and Techniques*, Vol. 46, No. 12, 1998, pp. 2053–2060. https://doi.org/10.1109/22.739282.

[39] Yang, X.-X., Jiang, C., Elsherbeni, A. Z., Yang, F., and Wang, Y.-Q., "A novel compact printed rectenna for data communication systems," *IEEE transactions on antennas and propagation*, Vol. 61, No. 5, 2013, pp. 2532–2539. https://doi.org/10.1109/TAP.2013.2244550.

[40] Koohestani, M., Tissier, J., and Latrach, M., "A miniaturized printed rectenna for wireless RF energy harvesting around 2.45 GHz," *AEU-International Journal of Electronics and Communications*, Vol. 127, 2020, p. 153478. https://doi.org/10.1016/j.aeue.2020.153478.

[41] Chawla, N., and Tosunoglu, S., "State of the art in inductive charging for electronic appliances and its future in transportation," *2012 Florida Conference on Recent Advances in Robotics*, 2012, pp. 1–7.

[42] Helmers, H., Lopez, E., Höhn, O., Lackner, D., Schön, J., Schauerte, M., Schachtner, M., Dimroth, F., and Bett, A. W., "68.9% Efficient GaAs-Based Photonic Power Conversion Enabled by Photon Recycling and Optical Resonance," *physica status solidi (RRL) – Rapid Research Letters*, Vol. 15, No. 7, 2021, p. 2100113. https://doi.org/10.1002/pssr.202100113.

[43] Olsen, L. C., Huber, D. A., Dunham, G., and Addis, F., "High efficiency monochromatic GaAs solar cells," *The Conference Record of the Twenty-Second IEEE Photovoltaic Specialists Conference-1991*, IEEE, 1991, pp. 419–424. https://doi.org/10.1109/PVSC.1991.169250.

[44] Green, M. A., Zhao, J., Wang, A., and Wenham, S., "45% efficient silicon photovoltaic cell under monochromatic light," *IEEE electron device letters*, Vol. 13, No. 6, 1992, pp. 317–318. https://doi.org/10.1109/55.145070.

[45] Bélanger, J., Venne, P., Paquin, J.-N., et al., "The what, where and why of real-time simulation," *Planet Rt*, Vol. 1, No. 1, 2010, pp. 25–29.

[46] Shin, K., and Ramanathan, P., "Real-time computing: a new discipline of computer science and engineering," *Proceedings of the IEEE*, Vol. 82, No. 1, 1994, pp. 6–24. https://doi.org/10.1109/5.259423.

[47] Lu, C., Saifullah, A., Li, B., Sha, M., Gonzalez, H., Gunatilaka, D., Wu, C., Nie, L., and Chen, Y., "Real-time wireless sensor-actuator networks for industrial cyber-physical systems," *Proceedings of the IEEE*, Vol. 104, No. 5, 2015, pp. 1013–1024. https://doi.org/10.1109/JPROC.2015.2497161.

[48] Boggia, G., Camarda, P., Grieco, L. A., and Zacheo, G., "A Real-time Wireless Communication System based on 802.11 MAC," *Factory Automation*, IntechOpen, 2010.

[49] Wei, Y.-H., Leng, Q., Han, S., Mok, A. K., Zhang, W., and Tomizuka, M., "RT-WiFi: Real-Time High-Speed Communication Protocol for Wireless Cyber-Physical Control Applications," *2013 IEEE 34th Real-Time Systems Symposium*, 2013, pp. 140–149. https://doi.org/10.1109/RTSS.2013.22.